BR

Michigan State University

National Superconducting Cyclotron Laboratory

A MEASUREMENT OF THE $^{8}Li(n,\gamma)^{9}Li$ CROSS SECTION AT ASTROPHYSICAL ENERGIES BY REVERSE KINEMATICS

P. ZECHER, A. GALONSKY, S.J. GAFF, J.J. KRUSE, G. KUNDE, E. TRYGGESTAD, J. WANG, R.E. WARNER, D.J. MORRISSEY, K. IEKI, Y. IWATA, F. DEÁK, Á. HORVÁTH, Á. KISS, Z. SERES, J.J. KOLATA, J. VON SCHWARZENBERG, and HUGO SCHELIN

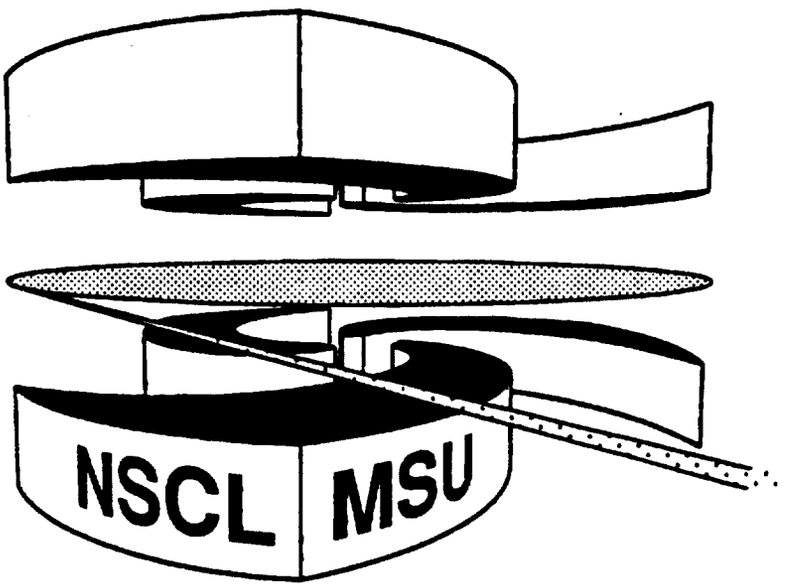

MSUCL-1080

AUGUST 1997

National Superconducting Cyclotron Laboratory. *PREPRINT* AUGUST 1997

A Measurement of the $^{8}Li(n,\gamma)^{9}Li$ Cross Section at Astrophysical Energies by Reverse Kinematics

P. D. Zecher*, A. Galonsky, S. J. Gaff, J. J. Kruse, G. Kunde, E. Tryggestad, J. Wang, R. E. Warner†
National Superconducting Cyclotron Laboratory and Department of Physics and Astronomy, Michigan State University, East Lansing, Michigan 48824

D. J. Morrissey
National Superconducting Cyclotron Laboratory and Department of Chemistry, Michigan State University, East Lansing, Michigan 48824

K. Ieki, Y. Iwata
Rikkyo University, 3 Nishi-Ikebukuro, Toshima, Tokyo 171, Japan

F. Deák, Á. Horváth, Á. Kiss
Department of Atomic Physics, Eötvös University, Puskin utca 5-7, H-1088 Budapest, VIII Hungary

Z. Seres
KFKI Research Institute for Particle and Nuclear Physics, 1525 Budapest 114 POB 49, Konkoly-These út 29-33, Hungary

J. J. Kolata, J. von Schwarzenberg
Department of Physics, University of Notre Dame, Notre Dame, Indiana 46556

and H. Schelin
CFET, Av. Sete de Setembro 3165 80230-901, Curitiba, Pr,Brazil

We have made the first attempt at determining the $^{8}Li(n,\gamma)^{9}Li$ cross section at astrophysical energies. This reaction competes with the $^{8}Li(\alpha,n)^{11}B$ reaction in the inhomogeneous big bang model and with ^{8}Li β-decay in the *r* process. It may affect the primordial abundance and the stellar production of A > 12 nuclei. Using a radioactive beam of ^{9}Li and the coulomb dissociation method we attempted to measure the cross section of the inverse reaction $^{9}Li(\gamma,n)^{8}Li$. We report only an upper limit because we were unable to determine and subtract nuclear dissociation. Through the detailed balance theorem, this lead to an upper limit for the cross section of interest, $^{8}Li(n,\gamma)^{9}Li$. The limit is 19±8 μb for E_n = 0-500 keV or, when expressed as a reaction rate, 7,200 $cm^3s^{-1}mole^{-1}$.

1. Introduction

The prediction of an inhomogeneous matter distribution during the early big bang [1] suggests that neutrons would diffuse from the high-density regions into the low-density regions because of their longer scattering length, creating proton-rich and neutron-rich regions of space. Nucleosynthesis in the proton regions would be similar to that in the standard big bang model, but in the neutron regions nucleosynthesis would be very different (see Figure 1). One possible result of neutron-rich nucleosynthesis is the production of observable amounts of A>12 nuclei by the *r* process. Once ^{7}Li is produced, the primary reaction chain to A>12 nuclei begins with $^{7}Li(n,\gamma)^{8}Li(\alpha,n)^{11}B$, with a weaker branch through $^{7}Li(a,\gamma)^{11}B$. A key reaction in determining the primordial abundances of A>12 nuclei is ^{8}Li neutron capture, which provides a leak from the primary reaction chain. Depending on the rate, this reaction could reduce A>12 production by as much as 50 percent [2].

* Present address: Deloitte & Touche Consulting Group, Two World Financial Center, New York, New York 10281-1420.

† Permanent address: Department of Physics, Oberlin College, Oberlin, Ohio 44074..

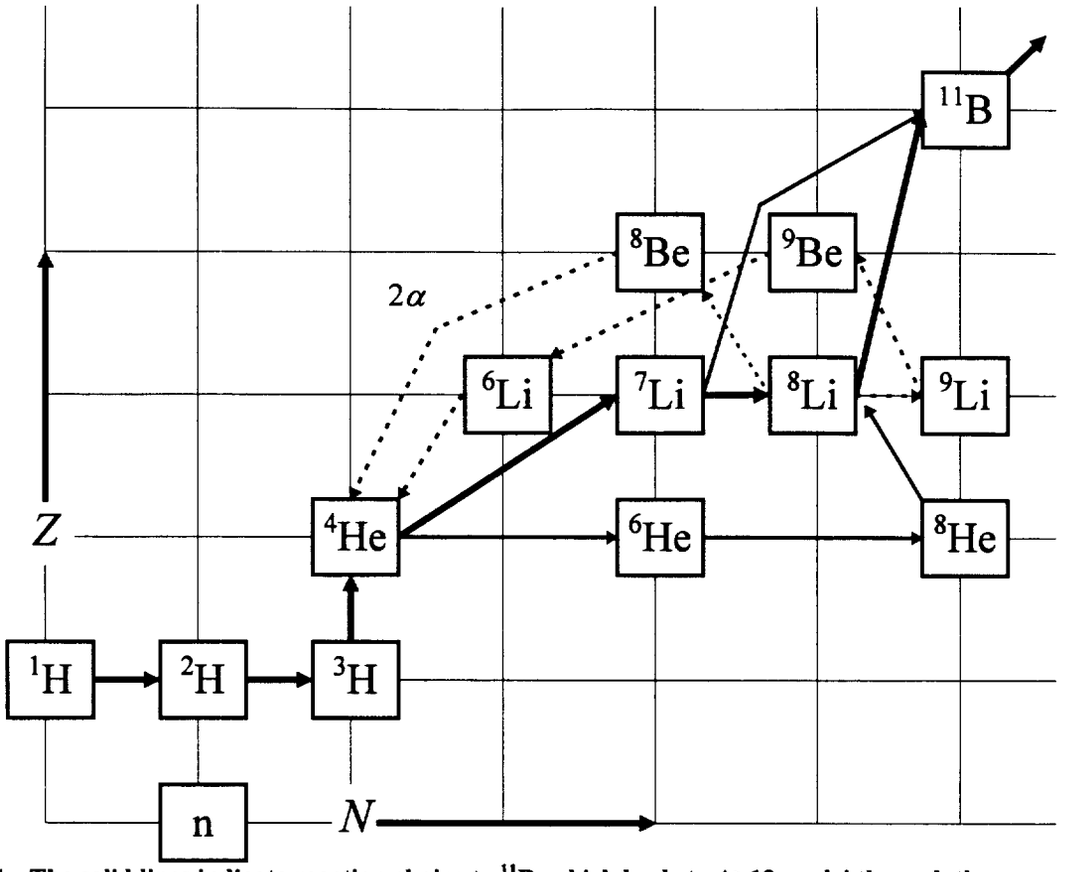

Figure 1 - The solid lines indicate reaction chains to ^{11}B, which leads to A>12 nuclei through the *r* process. The dashed lines indicate destructive chains leading to ^{4}He production.

The post-collapse phase of a Type II supernova may provide yet another opportunity for the *r* process to produce heavy isotopes [3-5]. Beginning in a He-rich environment the mass-8 gap would be bridged by either the triple-alpha process or the $\alpha+\alpha+n\rightarrow{}^{9}\mathrm{Be}$ reaction. The bridging reactions would continue until a neutron-rich freeze-out occurred, triggering the *r* process. If there was sufficient neutron abundance, it would also be possible to bridge the mass-8 gap through the reaction chain $^{4}\mathrm{He}(2n,\gamma)^{6}\mathrm{He}(2n,\gamma)^{8}\mathrm{He}(\beta^{-})^{8}\mathrm{Li}(n,\gamma)^{9}\mathrm{Li}$ [6] (see Figure 1). Such a reaction chain would start an alternative path that would proceed along the neutron-rich side of the line of stability. This chain could lead to significant production of ^{36}S, ^{40}Ar, ^{46}Ca, ^{48}Ca, isotopes whose origins are still uncertain. To what extent this chain competes with the $^{8}\mathrm{Li}(\beta^{-})^{8}\mathrm{Be}(2\alpha)$ decay chain depends on the neutron density and the cross section for the ^{8}Li(n,γ)^{9}Li reaction.

A number of theoretical estimates exist for the size of the ^{8}Li(n,γ)^{9}Li cross section. Some of the estimates are based on microscopic model calculations of the ^{8}Li structure [7,8]; others are estimates based on the systematics of similar nuclei [9,10]. These estimates vary by over an order of magnitude; consequently, the predicted abundance of A>12 nuclei remains very uncertain.

^{8}Li's half-life of less than 1 second probably makes a direct measurement of the capture cross section impossible. Fortunately, we can produce a beam of ^{9}Li nuclei, perform a measurement of the inverse reaction, $^{9}\mathrm{Li}+\gamma\rightarrow{}^{8}\mathrm{Li}+n$, and use the principle of detailed balance to deduce the cross section for the neutron capture reaction. The photons for the inverse reaction are obtained by passing the ^{9}Li through the virtual photon field near a high-Z nucleus such as Pb or U. This coulomb dissociation cross section is then related to the radiative capture cross section by [11]

$$\sigma_{(n,\gamma)}\left({}^8\mathrm{Li}+n\rightarrow{}^9\mathrm{Li}+\gamma\right)=\frac{2(2j_9+1)}{(2j_8+1)(2j_n+1)}\frac{k_\gamma^2}{k^2}\sigma_{(\gamma,n)}({}^9\mathrm{Li}+\gamma\rightarrow{}^8\mathrm{Li}+n)\,, \quad (1)$$

where k is the wave number for the ^{8}Li+n channel, k_γ is the photon wave number, and j_9, j_8, and j_n are the appropriate spins for ^{9}Li, ^{8}Li, and neutron respectively. Figure 2 shows a schematic drawing of the coulomb dissociation process. Using coulomb dissociation to study radiative capture reactions was first suggested by Baur, Bertulani and Rebel [12].

The photodisintegration cross section $\sigma_{(\gamma,n)}$ at energy E_γ can be determined from the measured differential coulomb excitation cross section $d\sigma/dE_\gamma$ as

$$\sigma_{(\gamma,n)}=\frac{E_\gamma}{n_{E1}}\frac{d\sigma}{dE_\gamma}\,, \quad (2)$$

where E_γ is the virtual photon energy and n_{E1} is the virtual photon number for electric dipole photons, which is calculable and assumed to dominate [12,13]. Since we have no control over the energy of the absorbed photon, it is necessary to measure it for each event. We get this from

$$E_\gamma = E_d + S_n\,, \quad (3)$$

where the decay energy E_d is the sum of the kinetic energies of the ^{8}Li fragment and the neutron in the ^{9}Li center of mass system, and S_n = 4.05 MeV is the neutron separation energy of ^{9}Li.

To determine E_d we make a complete kinematics measurement of the reaction products, the ^{8}Li fragment and the neutron, and get

$$E_d = \tfrac{1}{2}\mu V_{rel}^2\,, \quad (4)$$

where μ is the reduced mass, and $\mathbf{V}_{rel}$ is the relative velocity of the reaction products [14]. $\mathbf{V}_{rel}$ is the difference between the velocities in the ^{9}Li center of mass frame of the products, $\mathbf{V}_{rel} = \mathbf{V}_n - \mathbf{V}_{^8Li}$. Given that in the laboratory frame, $\mathbf{V}_n^{lab} = \mathbf{V}_n + \mathbf{V}_{^9Li}$ and $\mathbf{V}_{^8Li}^{lab} = \mathbf{V}_{^8Li} + \mathbf{V}_{^9Li}$, the relative velocity of the two products is also the difference between their laboratory velocities, $\mathbf{V}_{rel} = \mathbf{V}_n^{lab} - \mathbf{V}_{^8Li}^{lab}$. The laboratory velocities are determined by measuring the energy and direction of each reaction product.

We note that the virtual photons have a monotonically decreasing energy spectrum, and, with a minimum energy of 4.05 MeV, it is likely that nuclear dissociation will compete effectively with coulomb dissociation. Our planned procedure, therefore, was to measure the dissociation cross section for six different target nuclei with Z ranging from 6 to 92. For the lowest-Z targets, we expected the coulomb contribution to be negligible compared to the nuclear dissociation. We could then have used these cross sections to estimate the nuclear contribution of the higher-Z targets. Unfortunately, we did not obtain a sufficient yield from the low-Z targets to make any reasonable calculation of their

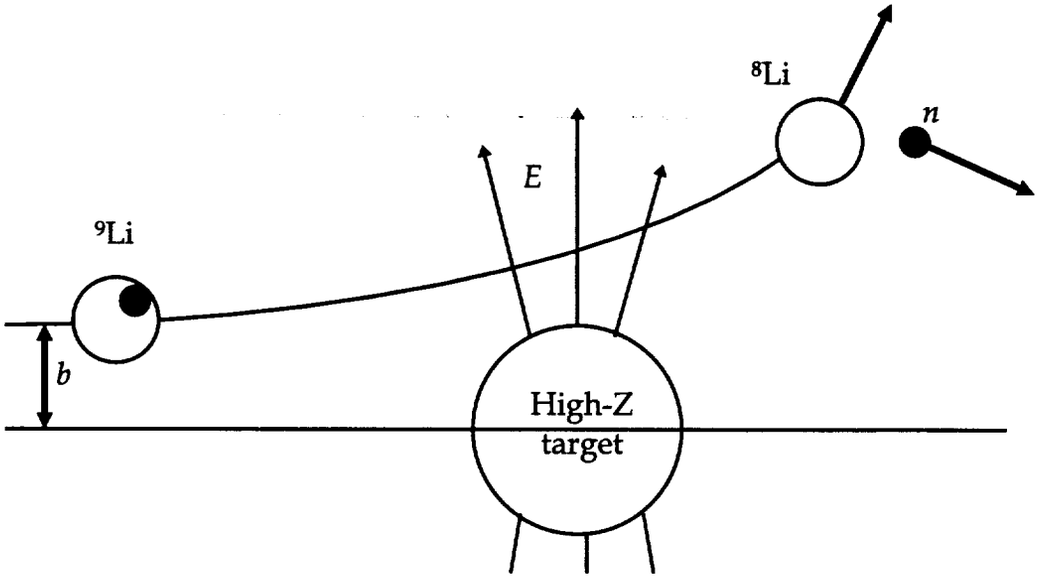

Figure 2 - Schematic drawing of the coulomb dissociation method.

dissociation cross section. As a result, we interpret our data from the two high-Z targets (see Table 1) as an upper limit to the coulomb dissociation, and thus report the neutron capture cross section also as an upper limit.

Table 1 - Target, thickness, and energy loss for 28.53 MeV/nucleon ^{9}Li particles.

Target	Thickness (mg/cm^2)	ΔE (MeV)
^{238}U	339.2	27.27
^{208}Pb	495.0	40.77

2. Experimental Setup

The measurements were performed at the National Superconducting Cyclotron Laboratory (NSCL). The laboratory's *A1200 Spectrograph* [15] was used to produce an isotopically pure beam of ^{9}Li by a fragmentation reaction of 60 MeV/nucleon ^{15}N on a thick ^{9}Be target. The beam of 28.53 MeV/nucleon ^{9}Li was sent into an experimental hall where, after passing through a target, the charged fragments were detected in a Si-CsI telescope and the neutrons were detected in the *Neutron Wall Array* [16].

Since big-bang nucleosynthesis begins when the temperature has dropped to $kT \approx 100$ keV, the ^{8}Li$(n,\gamma)^{9}$Li reaction is of astrophysical importance for neutrons of similar energy. Consequently, we were primarily interested in photodisintegrations with photon energies just above the binding energy 4.05 MeV. With a ^{9}Li beam energy of 28.53 MeV/nucleon, the beam velocity was much greater than the velocities of the decay products in the ^{9}Li rest frame; as a result, the decay products were forward focused in the laboratory.

To accommodate the forward focusing we placed both the fragment and neutron detectors at zero degrees with respect to the beam. The telescope was able to act as the beam stop because the beam current for the secondary radioactive beam was much less than a typical primary beam; for our ^{9}Li beam the rate was about 5000 per second. Unfortunately, the zero degree telescope provided more material in which the ^{9}Li could interact than did the target. To account for this effect, we made target-in and target-out measurements and subtracted the target-out yield from the target-in yield to observe the reactions from the target.

Figure 3 shows a schematic diagram of the experimental setup. The *A1200 Spectrograph* is not shown in the figure, nor is a small, thin plastic scintillator detector placed after the telescope and subtending the same solid angle as the *Neutron Wall Array*. This plastic scintillator was used to veto protons produced with enough energy to reach the *Neutron Wall Array*.

2.1. Fragment Telescope

The fragment telescope performed four functions: it identified the ^{8}Li fragments from among the unreacted ^{9}Li beam particles and other fragments and it provided the energy and angle of emission of

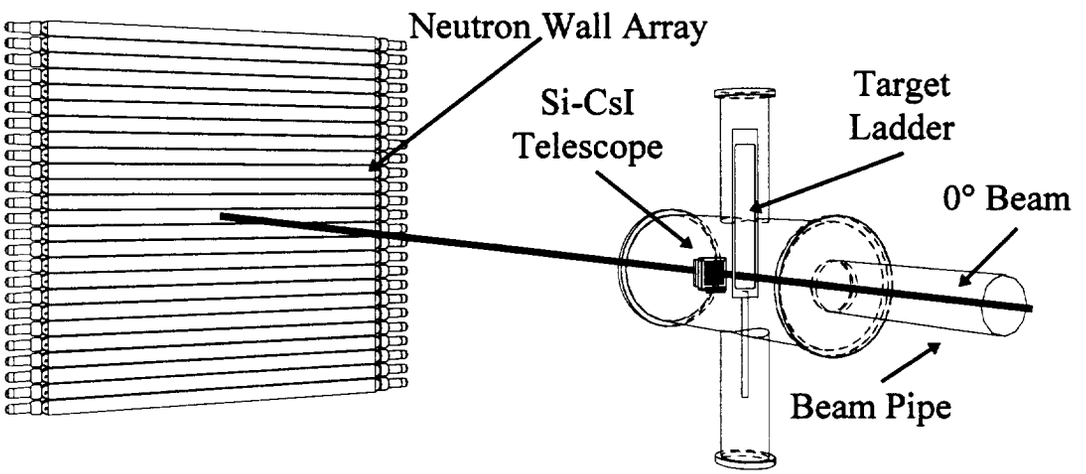

Figure 3 - A Schematic drawing showing the arrangement of the equipment. The Si-CsI telescope is 11.5 cm downstream from the target, and the center of the *Neutron Wall Array* is 5 meters downstream from the target.

each ^{8}Li. Its fourth function was to provide a timing signal that, in conjunction with a timing signal from the *Neutron Wall Array*, gives the neutron flight time from the target to the array. The particle identification is accomplished by using the technique of a ΔE-E telescope configured to determine both the mass and charge of the fragment [17].

The fragment telescope consisted of three individual detectors: a Si-strip detector 11.5 cm downstream from the target for transverse position, ΔE and timing information; a Si PIN diode detector for additional ΔE information; and a CsI stopping detector for residual energy information. Both Si detectors had an active area of 5x5 cm^2, and each was approximately 300 μm thick. The Si-strip detector had 16 vertical strips on one side and 16 horizontal strips on the other side. When a Li particle passed through the strip detector, most of the charge was collected on a single vertical strip and a single horizontal strip, thereby identifying the location of the event. The CsI detector was a 0.5-cm-thick square crystal, 6 cm on a side, and it was viewed by four Si-PIN diode detectors optically coupled to the back side of the crystal. By summing the ΔE signals from the Si detectors and comparing the sum to the energy deposited in the CsI detector, we identified the different fragment isotopes that entered the telescope.

The Si detectors were calibrated with both a ^{228}Th α-particle source and a series of calibration beams. The energy deposited in the Si detectors by the α-particles is independent of the thickness of the Si detectors because the α-particles' ranges are sufficiently smaller than the thickness. Conversely, each calibration beam passed through the Si detectors, and the energy deposited depended on the thickness of the detectors. By comparing the two calibrations, we were able to check the manufacturer's value of the thickness of each detector. The calibrated energy signals were summed to produce the ΔE value for the particle identification. The fragment's total energy was obtained by adding the ΔE value to the residual energy deposited in the CsI crystal. The measured energy resolution of the ΔE value was about 6% FWHM.

The light output of the CsI crystal, as a function of energy deposited, varies throughout the volume of the crystal. This produces very poor energy resolution when the crystal is viewed as a whole by the PIN diode detectors. To optimize the resolution, we used the pixel information from the Si strip detectors to calibrate 16 x 16 = 256 discrete regions of the CsI detector. Although the resolution still varied among regions, the mean resolution was 2.6% FWHM; the best region had a resolution of 1.5% FWHM and no region used in the analysis had a resolution worse than 3.0% FWHM. The errors from the Si detectors and the CsI detector combine in quadrature to give about 2.0% FWHM for the total fragment energy.

2.2. Neutron Wall Array

We detected the neutrons with the NSCL's *Neutron Wall Array* [16], a large, 2x2 m^2, position-sensitive neutron detector. Although the detector consists of two 2x2 m^2 planes, only one half of one plane was available at the time of the experiment. Each plane consists of an array of 25 2-m-long glass cells filled with a liquid scintillator, and the array is oriented so that the normal to the plane is parallel to the beam axis (see Figure 3). The cells are 7.62 cm high and 6.35 cm deep, and each cell is viewed by two photomultiplier tubes (PMT) optically coupled to the ends of the cell.

The primary mechanism for detecting neutrons with energies of 5–30 MeV is by observing the scintillation from a recoiling proton that has elastically scattered a neutron. The proton scintillation process cannot provide unique information about the incident energy of the neutron; therefore, it is necessary to use the time-of-flight (TOF) method to determine the energy of the incident neutron. When using the TOF method, the energy resolution is dependent on two factors: the intrinsic time resolution of the detector and the length of the flight path. The flight path was 5.07 meters from the target to the center of the array; this value was chosen as a balance between the acceptable solid angle subtended by the detector and the required energy resolution.

The *Neutron Wall Array* has a scintillator volume of about 500 liters, spread through two thin detecting planes with a very large surface area. This configuration makes it very sensitive to cosmic-ray and γ-ray backgrounds, since cosmic-ray efficiency is primarily dependent on the the detector's surface area. To eliminate this background, the *Neutron Wall Array* was built using the liquid scintillator NE-213, which has the well-known property of pulse-shape-discrimination (PSD), allowing us to distinquish between neutron events and γ-ray/cosmic-ray background events. Figure 4 demonstrates the PSD properties of the *Neutron Wall Array*. In this figure, an integral of the early part of the PMT signal, QFAST, is plotted against an integral of the total signal for events occuring along the entire length of the cell. To remove a position dependence caused by

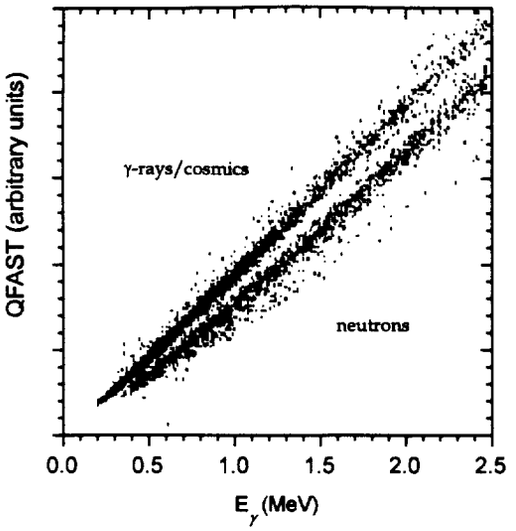

Fig. 4 - Low energy pulse-shape-discrimination spectrum for a cell in the Neutron Wall Array.

light absorption, we plot the square root of the product of the total signals from the two PMT signals on the abscissa and the square root of the product of the QFAST signals on the ordinate. The high quality PSD provided by the *Neutron Wall Array* was crucial to successfully executing this experiment.

The upper pane of Figure 5 shows the TOF spectrum for one cell in the neutron wall, including all γ-ray and cosmic-ray events. The TOF was measured between the Si-Strip detector and the mean-time of the two PMTs on the cell. It is not possible to know an exact zero for the clock from the electronics; therefore, we use the observed prompt γ-ray peak in the TOF spectrum to determine the time-equals-zero channel. The prompt γ-ray peak was produced when the *Neutron Wall Array* detected prompt γ-rays from nuclear interactions in the target and telescope. Since the γ-rays' flight time is independent of energy, and we know the flight path, we can determine when the clock started. The width of this peak is a measure of the intrinsic time resolution of the neutron detector and allows us to know the neutron energy resolution. For a 24-MeV neutron, over the 5-m flight path, the FWHM energy resolution is 3%. The lower pane of Figure 5 shows a neutron-only TOF spectrum for all the cells used during the experiment.

3. Analysis

The primary difficulty in the data analysis was identifying of the ^{8}Li particles in the telescope. Although the coincidence requirement with a neutron in the *Neutron Wall Array* eliminates all but a few of the ^{9}Li from the telescope spectrum, it was also necessary to distinguish the ^{8}Li from ^{7}Li, ^{4}He, and reaction products produced in the telescope itself.

When an interaction produced a detected neutron, it was difficult to determine whether the interaction took place in the target or the telescope. To remove this telescope background, we measured the cross section with the target and without the target, the so-called target-in and target-out measurements, and subtracted the target-out cross section from the target-in cross section. To avoid creating systematic errors between the two measurements, the beam energy for the target-out measurement was reduced by an amount equivalent to the energy loss in the targets.

To identify the ^{8}Li isotopes from the ΔE-E spectrum, we took advantage of the fact that light ions, such as He and Li, obey the empirical power-law formula $R = aE^{\alpha}$, where R is the range of a particle with an energy E, and a and α are constants [18]. Using this power-law relationship, a particle-

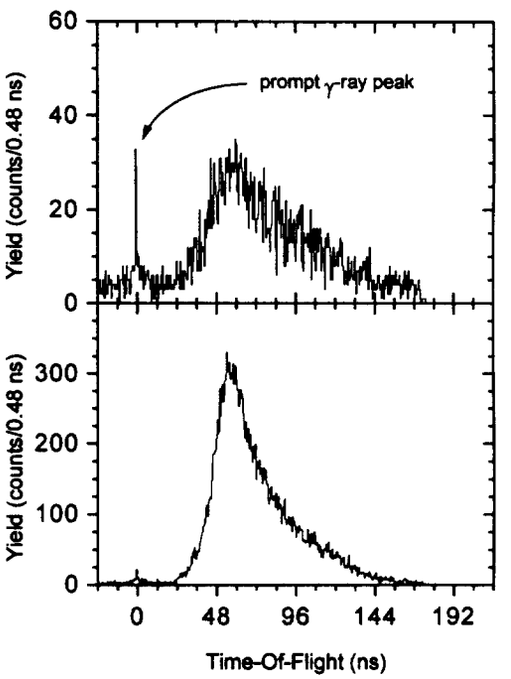

Figure 5 - Time-Of-Flight (TOF) spectra for the Neutron Wall Array. The upper pane shows the TOF spectrum for one cell without a neutron PSD filter applied to the data, the lower pane shows the TOF spectrum for all active cells with a neutron PSD filter.

identification (PID) function was derived [18] that is directly proportional to the mass and charge squared (AZ^2). The PID function is expressed as

$$\mathrm{PID} = E^{\alpha} - (E - \Delta E)^{\alpha} \qquad (5)$$

where E is the total energy of the fragment entering the Si-CsI telescope, ΔE is the energy loss in the Si detectors, and α is selected to provide a constant value of PID over the energy range of interest for a given fragment species. For our range of energy, values of α from 1.75 to 1.80 are acceptable. We used $\alpha = 1.78$.

The FWHM of the PID peak for a given isotope can be found from the widths of the individual detector resolutions and the two relations

$$E = E_{\mathrm{CsI}} + \Delta E \qquad (6)$$

and

$$\sigma^2_{\mathrm{PID}} = \alpha^2\left[\sigma^2_{E_{\mathrm{CsI}}}(E^{\alpha-1} - E^{\alpha-1}_{E_{\mathrm{CsI}}})^2 + \sigma^2_{\Delta E}E^{2(\alpha-1)}\right] \qquad (7)$$

The results are given in Table 2 for ^{9}Li and for its heavier dissociation products.

The upper pane of Figure 7 shows the PID spectrum for the lead target and for the target-out (telescope contribution); the lower pane shows the difference between the two spectra. Although the ^{8}Li yield was small, the ^{7}Li peak is clear enough that we were able to fit it to a gaussian distribution. Allowing all the parameters to vary, we obtained good agreement between the centroid (PID÷20) and width values in Table 2 and the fit results. The fit to the ^{8}Li peak shown is the result of fitting the ^{7}Li and ^{8}Li region of data to a double gaussian distribution, holding fixed the centroids and widths. (The ^{4}He peak is half way between the expected ^{4}He and ^{6}He peaks from Table 2; this is attributed to the non-linear response and projectile-Z dependence of the CsI light output.)

The large amount of ^{7}Li present in the spectrum was not expected. Given the complicated method of producing a ^{9}Li beam, it is natural to wonder whether the peak designated ^{7}Li was not actually ^{8}Li and the peak designated ^{8}Li was not actually unreacted ^{9}Li in chance coincidence with a neutron. To answer this, we analyzed the telescope events that were not in coincidence with an event in the *Neutron Wall Array*; their PID values were what we expected for ^{9}Li. We are thus confident that the calibrations are correct.

After using the PID value to identify the ^{8}Li fragments, we next used their total energy and direction from the target to determine their lab velocity, $\mathbf{V}^{\mathrm{lab}}_{Li}$. We did the same for the neutrons, and obtained $\mathbf{V}^{\mathrm{lab}}_{n}$. Using these values for each event, we determined the event's decay energy E_d from Eq. 4. The yields for decay-energy bins of width 0.5 MeV are shown in Figure 6 for the Pb and U targets. The error bars shown are statistical.

To obtain the dissociation cross section from this measured yield, we must know the efficiency of our detection system. Two factors constitute the detection efficiency: the intrinsic efficiency of each detector, and the geometrical acceptance of the detectors. The geometrical acceptance decreases with increasing decay energy, therefore, the efficiency must be folded with the decay energy distribution and cannot be simply applied to the total yield as a factor. Given that the intrinsic efficiency of the telescope was 100 percent, and using the simulation code TOTEFF [19] to determine the energy-dependent efficiency of the *Neutron Wall Array*, we used the monte carlo method to simulate various decay energies and the geometric acceptance of our apparatus to determine the overall energy-dependent efficiency.

Table 2 - Energy Losses, Particle Identification (PID) values and FWHM values of PID for ^{9}Li and for its heavier dissociation products.

Isotope	E (MeV)	E_{CsI} (MeV)	ΔE (MeV)	PID ÷20	$\mathrm{FWHM_{PID}}$ ÷20
^{9}Li	210	185.6	24.4	134.2	9.4
^{8}Li	185	160.4	24.6	121.6	8.5
^{7}Li	165	140.8	24.2	108.9	7.8
^{6}Li	140	115.6	24.4	95.4	6.6
^{8}He	185	174.1	10.9	55.7	3.8
^{6}He	140	129.2	10.8	44.2	3.1
^{4}He	95	84.3	10.7	31.7	2.1

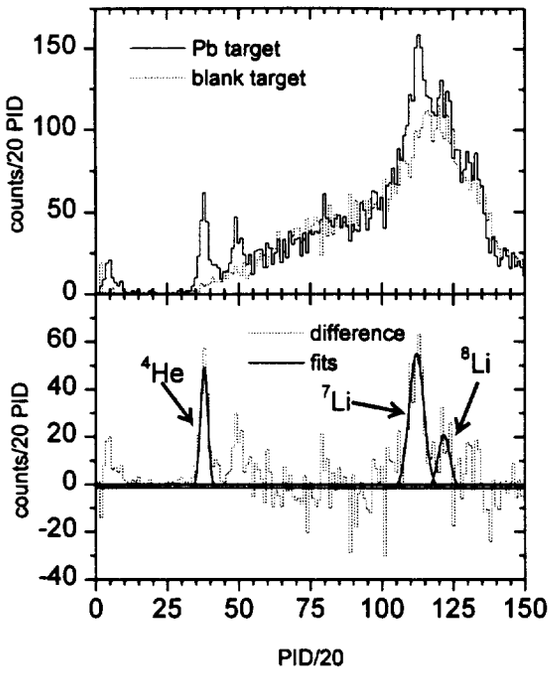

Figure 7 - The PID spectra for a Pb target. The upper pane shows the target in/target out data; the lower pane shows the difference of the two along with the best fits to a gaussian distribution for ^{4}He, ^{7}Li, ^{8}Li.

To determine the photodisintegration cross section from the measured dissociation cross section, we calculated the virtual photon spectrum for the Pb and U targets. The calculation and coulomb dissociation process are discussed at length in a review paper by Bertulani and Baur [13]. Sackett has shown that the relativistic approximation for the spectrum is valid for ^{11}Li in our velocity range [20], that there is little dependence on the projectile radius, and that the relativistic approximation is independent of the mass of the projectile. With this approximation the spectrum is given by

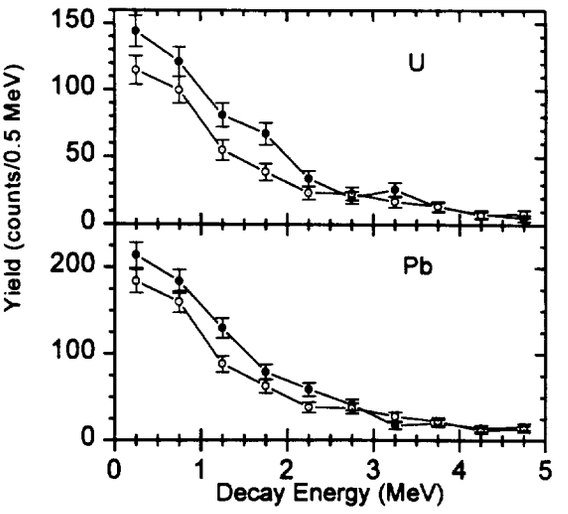

Figure 6 - Relative energy distributions for the U and Pb targets. The solid circles represent the target-in data and the open circles represent the target-out data.

$$n_{E1}\left(E_\gamma/\hbar\right)=\frac{2}{\pi}Z_T^2\alpha\left(\frac{c}{v}\right)^2\left\{xK_0K_1-\frac{1}{2}\left(\frac{v}{c}\right)^2x^2\left(K_1^2-K_0^2\right)\right\}, \tag{8}$$

where K_0 and K_1 are modified Bessel functions of the argument x, with $x=E_\gamma b_{\min}/\hbar\gamma v$. The minimum impact parameter, b_{min}, is the sum of the target and projectile radii.

4. Results

If Y is the ^{8}Li yield for some range of decay energy, then the measured dissociation cross section, $\sigma_{measured}$, is given by

$$\sigma_{measured}=\frac{Y}{\varepsilon N_T N_P}, \tag{9}$$

where ε is the detection efficiency for the measured decay energy, N_P is the number of incident ^{9}Li particles, and N_T is the number of target atoms per square centimeter. We obtain the differential cross section $d\sigma/dE_\gamma$ by dividing $\sigma_{measured}$ by the range of decay energies used to obtain $\sigma_{measured}$ Then, with the extreme assumption that all of $\sigma_{measured}$ results from coulomb dissociation, $\sigma_{(\gamma,n)}$ is found using Eq. 2,

$$\sigma_{(\gamma,n)}=\frac{E_\gamma}{n_{E1}}\frac{d\sigma}{dE_\gamma}. \tag{3}$$

Finally, we use the detailed balance theorem Eq. 1 to calculate the radiative capture cross section, ^{8}Li(n,γ)^{9}Li. Table 3 shows the results of these calculations. For each target, two decay energy bins, each 0.5 MeV wide, from 0 to 1.0 MeV, were considered.

Although we have only been able to determine an upper limit to the radiative neutron capture cross section for ^{8}Li, it is still of some use for its astrophysical implications considering the large range of theoretical estimates. These estimates are shown in Figure 8 along with our measured limits from the Pb and U targets. The estimates shown are for the direct capture to the ground state unless otherwise noted. We compare our data only to the ground state capture since the ^{9}Li is in its ground state when we measure the inverse reaction ^{9}Li(γ,n)^{8}Li. Direct capture to the ground state should be stronger than to the one bound excited state at 2.69 MeV [21] since the transition strength goes as E_γ^3.

A neutron-unbound state exists in ^{9}Li at 4.31 MeV, 0.247 MeV above the neutron decay threshold. Although there are no experimental determinations of this state's spin-parity [21], two shell-model calculations by Mao and Champagne [2] predict it to be $J^\pi = 5/2^-$. Given this spin-parity, p and f waves are required to form the resonance by neutron capture. Since neutrons around 0.247 MeV are primarily s-wave, the resonance is not expected to contribute much to the cross section. Also, γ-ray transitions from this excited state are through E2 rather than E1 radiation, further suppressing its contribution.

Of the four theoretical estimates shown, two are based on models of the ^{9}Li structure, and two are based on the systematics of similar nuclei. Of the model calculations, we are in sharp disagreement with the spd-shell model calculations of Mao & Champagne [7] and consistent as an upper limit with the cluster model calculations of Descouvemont [8]. For the estimates based on systematics, we are in disagreement with the estimates of Malaney & Fowler [10], and consistent with the estimates of Rauscher *et al.* [9].

Considering their astrophysical interest, radiative capture cross sections are often discussed in terms of a reaction rate per particle pair, $N_A\langle\sigma v\rangle$, where N_A is Avogadro's number, and $\langle\sigma v\rangle$ is given by

$$\langle\sigma v\rangle = \int_0^\infty \phi(v)\sigma(v)v\,dv, \qquad (10)$$

where $\phi(v)$ is the normalized Maxwell-Boltzman distribution, $\sigma(v)$ is the cross section, and v is the relative velocity. This reaction rate is approximately constant for low-energy, s-wave neutron capture because the cross section for the direct capture of s-wave neutrons is proportional to $1/v$. By fitting a $1/v$ function to our data points, we obtain an upper limit to the reaction rate, $N_A\langle\sigma v\rangle < 7{,}200$ cm^3 s^{-1} mole^{-1}. This rate, and the four theoretical estimates, are given in Table 4.

Table 4 - Reaction rates for the four theoretical estimates and our data.

	Reaction Rate cm^3 s^{-1} mole^{-1}
Malaney & Fowler [10]	4.29×10^4
Mao & Champagne [7]	2.10×10^4
NSCL-MSU	$< 0.72\times10^4$
Descouvemont [8]	0.53×10^4
Rauscher, *et al.* [9]	0.47×10^4

5. Conclusions

In an inhomogeneous early universe, nucleosynthesis in neutron-rich regions could produce an observable amount of A > 12 isotopes, whereas the standard big-bang nucleosynthesis ends with the production of ^{7}Li. The primary reaction chain to heavy elements begins with ^{7}Li(n,γ)^{8}Li(α,n)^{11}B and has a weaker channel beginning with ^{7}Li(α,γ)^{11}B.

Table 3 - Radiative capture cross section calculated from the detailed balance theorem.

Target	Decay Energy (MeV)	Observed Counts		$\sigma_{measured}$ (mb)	(mb)	$n(E_\gamma)$	$\sigma_{(\gamma,n)}$ (mb)	(mb)	(upper limit) $\sigma_{(n,\gamma)}$ (μb)	(μb)
U	0.0-0.5	29.4	±16.1	13.9	±7.6	225.44	0.53	±0.3	19.1	±10.4
U	0.5-1.0	21.2	±14.9	10.2	±7.1	186.05	0.53	±0.4	7.9	±5.5
Pb	0.0-0.5	29.9	±20.0	10.8	±7.2	188.56	0.50	±0.3	17.8	±11.9
Pb	0.5-1.0	23.6	±18.6	8.7	±6.9	154.16	0.54	±0.4	8.1	±6.4

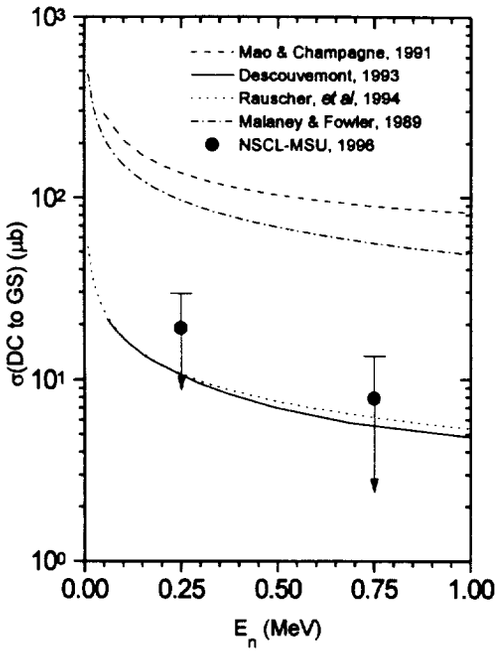

Figure 8 - Radiative capture cross sections for ^{8}Li(n,γ)^{9}Li. The data points are upper limits measured using the coulomb dissociation method with Pb and U targets. All curves are for direct capture to the ground state, except Malaney & Fowler [10], which is for direct capture to the ground state and first-excited state.

The ^{8}Li(n,γ)^{9}Li reaction provides a so-called leak from the primary chain, reducing the heavy-element production. This leak could reduce the heavy-element production by one-half according to Malaney & Fowler [2]. Our data suggest that the reduction might not be so large.

We used the coulomb dissociation method to determine an upper limit to the ^{8}Li(n,γ)^{9}Li radiative capture cross section. The very small yield from low-Z targets prevented us from making any estimate of the nuclear contribution to the measured dissociation cross section from high-Z targets. Without this estimate, our measurement can only be interpreted as an upper limit. Even so, two of the current predictions of this cross section are inconsistent with our measurement.

6. Acknowledgments

The authors would like to thank Michael Wiescher of the University of Notre Dame for helpful discussions. They are grateful for financial support from the U.S. National Science Foundation under Grant Numbers PHY93-14992, INT-13997 and PHY94-23659, from the Hungarian Academy of Sciences under Grant OTKA 2181, and from the Ministry of Education, Science, Sports and Culture of Japan under Grant numbers 07640421, 08640392 and 08044095.

References

[1] E. Witten, Phys. Rev. D **30**, 272 (1984).
[2] R. A. Malaney and W. A. Fowler, in *The Origin and Distribution of the Elements*, edited by G. J. Mathews (Singapore: World Scientific, 1988), p. 76.
[3] S.E. Woolsey and R.D. Hoffman, Astrophys. J. **395**, 202 (1992).
[4] B.S. Meyer, W.M. Howard, G.J. Mathews, S.E. Woolsey and R.D. Hoffman, Astrophys. J. **399**, 695 9!992).
[5] S.E. Woosley, J.R. Wilson, G.J. Mathews, R.D. Hoffman and B.S. Meyer, Astrophys. J. **433**, 229 (1994).
[6] J. Görres, H. Herndl, I.J. Thompson and M. Wiescher, Phys. Rev. C **52**, 2231 (1995).
[7] Z. Q. Mao and A. E. Champagne, Nucl. Phys. **A522**, 568 (1991).
[8] P. Descouvemont, Astrophys. J. Lett. **405**, 518 (1993).
[9] T. Rauscher, J. H. Applegate, J. J. Cowan, F. K. Thielemann, and M. Wiescher, Astrophys. J. **429**, 499 (1994).
[10] R. A. Malaney and W. A. Fowler, Astrophys. J. **345**, L5 (1989).
[11] R.G. Sachs, *Nuclear Theory* (Addison-Wesley Publishing Company, Inc., 1953), p. 141.
[12] G. Baur, C.A. Bertulani and H. Rebel, Nucl. Phys. **A458**, 188 (1986).
[13] C. A. Bertulani and G. Baur, Physics Reports **163**, 302 (1988).
[14] L. Heilbronn, A. Galonsky, X. Yang, F. Deák, Á. Kiss, and Z. Seres, Phys. Rev. C **40**, 2576 (1989).
[15] B.M. Sherrill, *et al.*, Nucl. Instrum. Methods **B 70**, 289 (1992).
[16] P.D. Zecher *et al.*, Nucl. Instrum. Methods, in press.
[17] G. W. Butler, A. M. Poskanzer and D. A. Landis, Nucl. Instrum. Methods **89**, 189 (1970).
[18] F.S. Goulding, D.A. Landis, J. Cerny and R.H. Pehl, Nucl. Instrum. Methods **31**, 1 (1964).
[19] R. Kurz, computer code TOTEFF, University of California Report UCRL-11339, unpublished (1964), modified for NE-213 by R. Doering, Ph.D. dissertation, Michigan State University (1974).
[20] D. Sackett, Ph.D. dissertation, Michigan State University, 1992.
[21] F. Ajzenberg-Selove, Nucl. Phys. **A490**, 1 (1988).